

# Study of quark and gluon jet identification in photoproduction at EIC

Siddharth Narayan Singh\*  
Brandeis University, Waltham, US

R. Aggarwal†  
USAR and USBAS, Guru Gobind Singh Indraprastha University, East Delhi Campus, 110092, India

M. Kaur‡  
Department of Physics, Panjab University, Chandigarh 160014, India  
Department of Physics, Amity University, Punjab, Mohali 140306, India  
(Dated: March 11, 2026)

## Abstract

We investigate the substructure of jets produced in photoproduction events with center-of-mass energies  $\sqrt{s} = 30\text{--}140$  GeV at the proposed Electron-Ion Collider (EIC). Events are generated using PYTHIA and contributions from direct and resolved photoproduction subprocesses are analyzed at different center-of-mass energies. Jets are reconstructed using longitudinally invariant  $k_T$  algorithm within the FastJet framework. Substructure of quark- and gluon-initiated jets in the selected di-jet photoproduction sample is studied in detail by using jet-shape variables. Predictions for subjet multiplicities and integrated jet shapes are presented in the gluon-initiated and quark-initiated jets. These results demonstrate the feasibility of distinguishing quark and gluon jets in the photo-production events at the EIC and provide a baseline for further QCD studies.

## I. INTRODUCTION

Jets are regarded as an important observable signal of quarks or gluons inside nucleons. The parton that initiates the showering is usually associated with the type of jet at the leading order (LO), though there is no single or unique way of classifying quark and gluon jets [1, 2]. In the LO quantum chromodynamics (QCD), gluons have a higher probability of radiating soft gluons compared to quarks and hence it is intuitive to find differences in the quark and gluon jet substructures [3–11]. At large transverse jet energies, where the fragmentation effects are small, the jet substructure is governed largely by the initiating partons [12–15].

Quarks and gluons, due to asymptotic freedom of QCD, behave as quasi-free particles at short distances of the order of  $10^{-15}$  cm. The observation of quark and gluon jets was crucial in establishing QCD as Standard Model's theory of the strong interactions. At short distances, the jets which are narrowly collimated bundles of hadrons, reflect quark and gluon configurations. The study of separating quark and gluon jets is important because it increases the viability and precision of numerous physics studies at the present and upcoming high-energy colliders [16–22]. The studies involving the beyond standard model (BSM) physics where signals would be hidden in the form of quark jets in the Standard Model background of gluon jets, such a classification would be important [22, 23]. Various methods including both physical observables and modern machine learning techniques [24–34] have been used for this purpose.

This paper presents the characteristic features of quark and gluon jets: quark jets are narrow and collimated, whereas gluon jets exhibit wider dispersion due to their larger color factor, which enhances soft gluon radiation. A detailed systematic study of jet identification is presented in  $ep$  photoproduction events generated using PYTHIA [35], considering the kinematic reach of the proposed EIC experiment. The transverse energy profiles of quark and gluon jets are studied through their differential and integrated jet-shape distributions. The integrated jet shape can be defined as the average fraction of the jet's transverse energy  $E_T$  contained inside a cone of radius  $r$  centred on the jet axis. The present study emphasizes the utility of jet substructure analysis, specifically through the integrated jet shape variable  $\Psi(r)$ , to distinguish between gluon-initiated and quark-initiated jets by labelling them as thick and thin jets respectively. A comparison is made between the jet shapes obtained at EIC and with the corresponding results from HERA, the first and only  $ep$  collider. This serves as a reference for future EIC jet measurements. Such an analysis has not been performed previously in the EIC framework.

Using the differences observed in integrated jet shapes between quark and gluon jet subsamples, selection cuts have been devised for the future EIC experiment that can be useful for producing quark-enriched and gluon-enriched jet samples. Investigating the internal structure of jets provides insight into the transition from a parton produced in a hard process to the experimentally observable spray of hadrons [36, 37]. The Jet substructure [38–43] can be probed to understand the underlying physics of the collision. The number of jet-like substructures resolved within jets by reapplying the jet algorithm at a smaller resolution scale  $y_{\text{cut}}$  is known as subjet multiplicity. In this paper, a systematic comparison of subjet multiplicities in quark and gluon jets is presented using

\* siddharthsingh@brandeis.edu

† ritu.aggarwal1@gmail.com

‡ manjit@pu.ac.in

photoproduction processes at proposed EIC energies.

The results are useful for comparison with data and for constraining non-perturbative effects through improved event generator tuning. At the EIC, jets are expected to serve as precise probes for initial data collection from lepton-nucleus collisions [44], anticipated to yield cleaner results than those from hadron beam experiments. This highlights the importance of the presented analysis, as well as to investigate the feasibility of jet classification and production of quark-enriched and gluon-enriched jet samples using photoproduction processes at various EIC energies.

This paper is structured as follows. Section 2 covers event generation and the event sample selection procedure. Section 3 introduces the jet algorithm used for jet reconstruction and examines jet shape observables, namely differential jet shape, integrated jet shape, and subjet multiplicity. The use of these observables to discriminate quark and gluon jets is described in Section 4. An outlook on the proposed EIC experiment in view of this analysis is discussed in Section 5, followed by conclusion in Section 6.

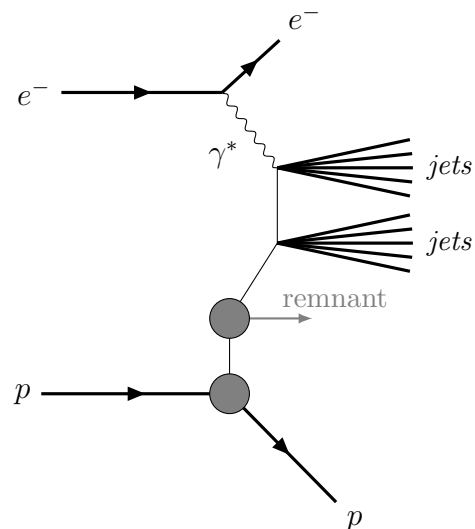
## II. EVENT GENERATION AND SELECTION

Table I. Beam energies of colliding particles, the corresponding center-of-mass,  $\sqrt{s}$  energies and the number of events generated for simulating collisions at the EIC and HERA.

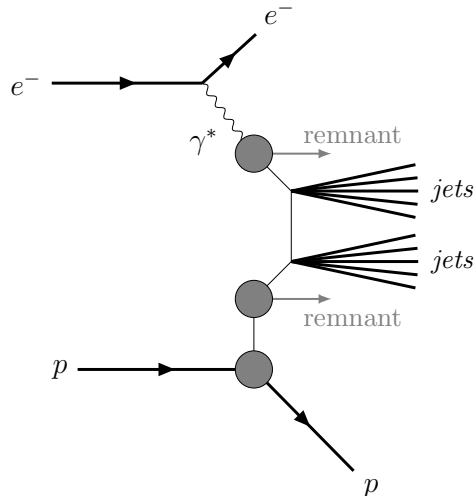
Beam energies (GeV)	$\sqrt{s}$ (GeV)	Events
EIC (10, 100)	63.2	998,511
EIC (10, 275)	104.9	999,444
EIC (18, 275)	141	999,633
HERA (27.5, 820)	300	999,881

The Monte Carlo event generator PYTHIA v8.309 [35] is used to simulate  $ep$  photoproduction events at low four-momentum transfers, with  $10^{-5} < Q^2 < 1.0 \text{ GeV}^2$ . At leading order (LO), photoproduction events can be broadly classified into direct and resolved processes, as shown in Figs. 1(a) and (b), respectively. In the direct photon-parton interaction, the photon acts as a point-like particle, interacting either with a quark inside the proton via QCD Compton scattering ( $\gamma q \rightarrow gq$ ), or with a gluon via boson-gluon fusion ( $\gamma g \rightarrow q\bar{q}$ ). In the resolved process, the photon exhibits a partonic structure that interacts with partons from the hadron ( $qq \rightarrow qq$ ,  $q\bar{q} \rightarrow q\bar{q}$ ,  $q\bar{q} \rightarrow gg$ ,  $gg \rightarrow q\bar{q}$ ,  $gg \rightarrow gg$ ,  $gq \rightarrow gq$ ; charge conjugates included). Both direct and resolved subprocesses are simulated.

The events are generated at three different center-of-mass energies of the proposed future EIC experiment as listed in the Table I. For the validation of the study and the comparison of the results, events are also simulated for  $\sqrt{s}=300 \text{ GeV}$  corresponding to the published HERA



a. Direct Photoproduction Process



b. Resolved Photoproduction Process

Figure 1. Direct (a) and Resolved (b) Photoproduction Processes

data [45]. A comparison of the direct and resolved subprocesses generated in the samples at various center-of-mass energies is given in Table II. The resolved processes are dominated by the presence of a quark jet and a gluon jet in the final state, whereas in the direct process two quark jets in the final state dominate. The percentage of direct events increases from about 26% at  $\sqrt{s}=300 \text{ GeV}$  to about 50% at  $\sqrt{s}=64 \text{ GeV}$ .

To validate the analysis procedure, photoproduction events were simulated at HERA energies and compared with published HERA results [45]. The data were best described with  $p_{T0}^{\text{ref}} = 3.0 \text{ GeV}/c$ , where  $p_{T0}^{\text{ref}}$  is a key parameter in the PYTHIA tune, closely tied to choices such as color flow description [35]. This value lies between those optimal for  $\gamma\gamma$  and  $pp$  collisions, reflecting the photon's cleaner partonic structure compared to the proton, or indicating that more sophisticated en-

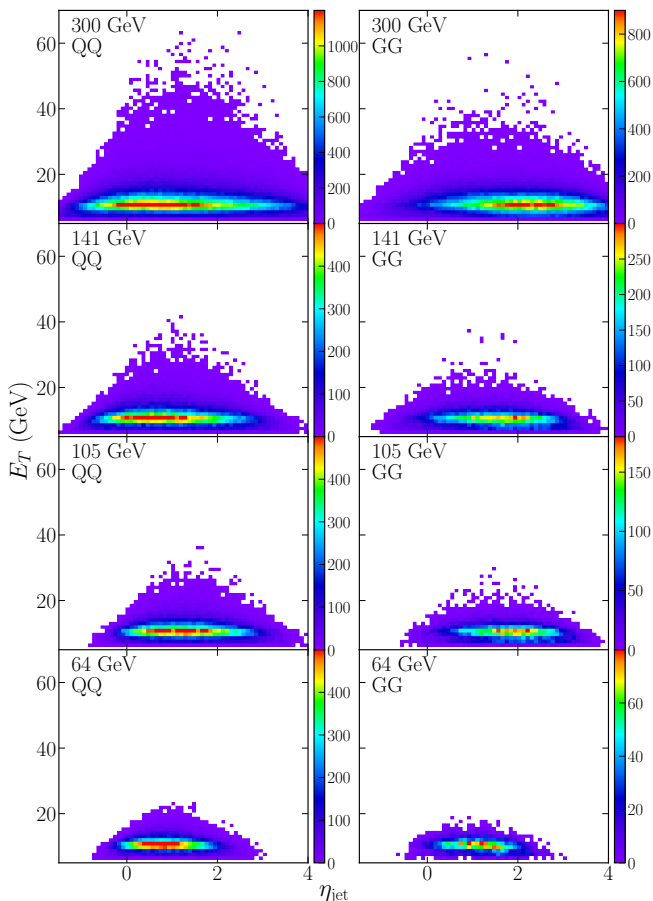


Figure 2. The  $E_T$  and  $\eta$  distribution of jets in the generated GG and QQ dijet photoproduction subsamples.

ergy scaling of  $p_{T0}(\sqrt{s})$  may be required. The parameter `PhaseSpace:pTHatMin` sets the minimum partonic transverse momentum in the hard  $2 \rightarrow 2$  scattering process before parton showering and hadronization, serving as an infrared cutoff to avoid regions where perturbative QCD becomes unreliable. The PYTHIA photoproduction examples use `PhaseSpace:pTHatMin` = 5.0 GeV as a standard choice for hard scattering studies [35]. The present analysis uses a lower value of `PhaseSpace:pTHatMin` = 3 GeV to access softer processes relevant for jet shape studies. Both  $p_{T0}^{\text{ref}}$  and `PhaseSpace:pTHatMin` should be tuned for future EIC studies when comparisons with real data become available.

### III. JETS

In particle collisions, a jet is a collimated spray of hadrons produced when a high-energy parton fragments and hadronizes. Jets are formed from these final-state hadrons and typically consist of a large number of particles traveling in roughly the same direction. Several jet algorithms have been developed over the years, each possessing its own strengths and weaknesses. These in-

Table II. Photoproduction cross sections and subprocess contributions for different center-of-mass energies. Only the dominant subprocess contributions are shown for clarity. Minor contributions (< 1% each) are included in the total cross sections.

Subprocess	Contribution
<b>EIC 64 GeV</b>	
<b>Resolved</b>	<b>3.23 nb, 50.2 %</b>
$qg \rightarrow qg$	27.09 %
$qq \rightarrow qq$	16.47 %
$gg \rightarrow gg$	5.42 %
<b>Direct</b>	<b>3.21 nb, 49.8 %</b>
$q\gamma \rightarrow qg$	26.73 %
$\gamma g \rightarrow q\bar{q}$	14.29 %
<b>EIC 105 GeV</b>	
<b>Resolved</b>	<b>13.63 nb, 62.6 %</b>
$qg \rightarrow qg$	35.26 %
$qq \rightarrow qq$	15.81 %
$gg \rightarrow gg$	10.33 %
<b>Direct</b>	<b>8.16 nb, 37.4 %</b>
$q\gamma \rightarrow qg$	16.24 %
$\gamma g \rightarrow q\bar{q}$	12.91 %
<b>EIC 141 GeV</b>	
<b>Resolved</b>	<b>5.71 nb, 61.4 %</b>
$qg \rightarrow qg$	34.66 %
$qq \rightarrow qq$	16.62 %
$gg \rightarrow gg$	8.92 %
<b>Direct</b>	<b>3.59 nb, 38.6 %</b>
$q\gamma \rightarrow qg$	16.80 %
$\gamma g \rightarrow q\bar{q}$	12.74 %
<b>HERA 300 GeV</b>	
<b>Resolved</b>	<b>33.67 nb, 74.4 %</b>
$qg \rightarrow qg$	42.36 %
$gg \rightarrow gg$	17.37 %
$qq \rightarrow qq$	13.48 %
<b>Direct</b>	<b>11.61 nb, 25.6 %</b>
$\gamma g \rightarrow q\bar{q}$	10.15 %
$q\gamma \rightarrow qg$	8.10 %

clude sequential clustering algorithms – such as  $k_T$ , anti- $k_T$ , and Cambridge/Aachen as well as traditional cone algorithms. A detailed comparison of these different jet algorithms is provided in Refs. [46].

In this study, jets are reconstructed using the longitudinally invariant  $k_T$  sequential recombination algorithm [47], implemented with FastJet v3.4.0 [48], with jet radius  $R = 1.0$ . The formulation of the longitudinally invariant  $k_T$  jet algorithm is summarized as follows:

- In the traditional  $k_T$  algorithm, clustering is based on both transverse momentum and the distance in the pseudorapidity-azimuthal angle space. However, this definition makes the algorithm sensitive to boosts along the longitudinal direction. To overcome this limitation, the longitudinally invariant  $k_T$  algorithm [47] modifies the distance measure to ensure independence from the

longitudinal direction. It specifically employs the following distance measures:

$$d_{ij} = \min(p_{T,i}^2, p_{T,j}^2) \frac{\Delta R_{ij}^2}{R^2} \quad (1)$$

$$d_{iB} = p_{T,i}^2 \quad (2)$$

where  $p_{T,i}$  and  $p_{T,j}$  are the transverse momenta of particles  $i$  and  $j$ ,  $\Delta R_{ij}^2 = (y_i - y_j)^2 + (\phi_i - \phi_j)^2$  is the squared distance in the rapidity-azimuthal angle plane,  $R$  is the jet radius parameter, and  $d_{iB}$  is the beam distance.

- The algorithm iteratively finds the minimum distance  $d_{\min}$  among all  $d_{ij}$  and  $d_{iB}$ . If the minimum is  $d_{ij}$ , particles  $i$  and  $j$  are merged into a single cluster. If the minimum is  $d_{iB}$ , particle  $i$  is declared a jet and removed from the list.

The analysis focuses on two-jet events, where the jet with the highest transverse energy  $E_T$  is classified as the leading jet, and the jet with the second-highest  $E_T$  is designated as the associated jet. The selection criteria require the leading jet to have  $E_T > 10$  GeV and the associated jet to have  $E_T > 7$  GeV.

Table III. Event counts and fraction information for photo-production at different center-of-mass energies. Event data represents a sample of two-jet events from PYTHIA8 Monte Carlo simulation output.

Event Type	Count	Fraction (%)
<b>EIC 64 GeV</b>		
QQ Events	401,596	40.22
GG Events	58,928	5.90
GQ Events	537,987	53.88
<b>EIC 105 GeV</b>		
QQ Events	378,245	37.84
GG Events	107,066	10.71
GQ Events	514,133	51.45
<b>EIC 141 GeV</b>		
QQ Events	391,413	39.16
GG Events	93,259	9.33
GQ Events	514,961	51.51
<b>HERA 300 GeV</b>		
QQ Events	318,964	31.90
GG Events	176,498	17.65
GQ Events	504,451	50.45

Based on the parton-level information from PYTHIA, the two-jet final states in the generated samples are classified into three categories: QQ events (both jets initiated by quarks), GG events (both jets initiated by gluons), and QG events (one quark jet and one gluon jet). The

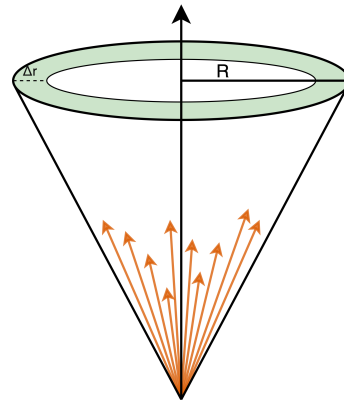


Figure 3. The differential jet shape is the average fraction of the jet's transverse energy  $E_{T,jet}$  contained inside an annulus of radius  $r$ , centred around the jet-axis.

relative fractions of these event types at various center-of-mass energies are summarized in Table III. Figure 2 shows the transverse energy  $E_T$  and pseudorapidity  $\eta$  distributions for jets in the GG and QQ subsamples, where events are required to have exactly two reconstructed jets. The properties of jets from these samples are studied in the following subsections, beginning with the energy distribution within jets and progressing to substructure through subjet analysis.

## A. Jet properties

The internal structure of a jet can be characterized using several observables that probe different aspects of the energy and particle distributions within the jet [38]. Two primary categories of jet shape observables are commonly employed: differential jet shapes, which measure the transverse energy density in annular rings at fixed radial distances from the jet axis, and integrated jet shapes, which quantify the cumulative energy fraction within a cone of given radius. Complementary information is provided by subjet multiplicity, which counts the number of resolved substructures within a jet at a given resolution scale [42].

### 1. Differential Jet Shape

The differential jet shape is defined as the mean proportion of a jet's transverse energy that is located within an annular region of radii  $r \pm \Delta r/2$ , concentric with the jet axis in the  $\eta$ - $\phi$  plane as shown in Figure 3.

$$\rho(r) = \frac{1}{N_{jets}} \frac{1}{\Delta r} \sum_{Jet} \frac{E_T(r - \Delta r/2, r + \Delta r/2)}{E_T(0, r = 1)} \quad (3)$$

where,  $N_{jets}$  is the number of jets in the sample and  $E_T(r - \Delta r/2, r + \Delta r/2)$  is the transverse energy within the given annulus of thickness,  $\Delta r = 0.1$ . Here,  $r$  is a

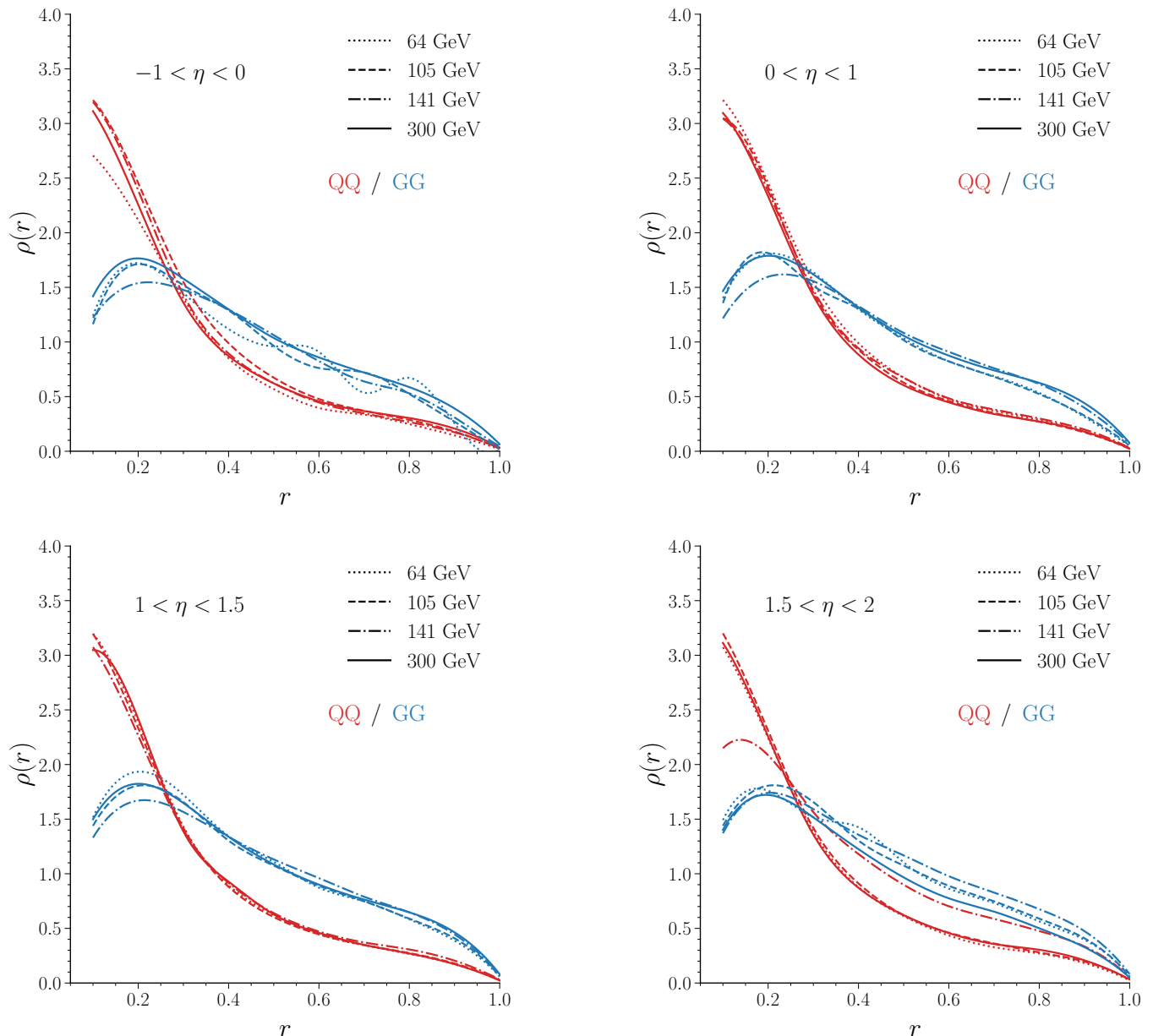


Figure 4. Differential jet shape distribution  $\rho(r)$  for GG (blue) and QQ (red) dijet photoproduction subsamples at different  $ep$  energies in four pseudorapidity bins:  $-1 < \eta < 0$  (top left),  $0 < \eta < 1$  (top right),  $1 < \eta < 1.5$  (bottom left), and  $1.5 < \eta < 2$  (bottom right).

non-dimensional parameter that facilitates the comparison of jet profiles at different radial distances from the jet-axis. The differential jet shape distributions  $\rho(r)$  for GG and QQ photoproduction subsamples in  $ep$  collisions across four pseudorapidity bins:  $-1 < \eta < 0$ ,  $0 < \eta < 1$ ,  $1 < \eta < 1.5$ , and  $1.5 < \eta < 2$  are shown in Fig. 4.

It is observed that for quark jets,  $\rho(r)$  peaks sharply near the jet axis, indicating that most of the jet's energy is concentrated in a narrow core. In contrast, gluon jets exhibit a flatter  $\rho(r)$  distribution, with more energy deposited at larger radii, resulting in a broader jet profile. This difference arises from the distinct color charges of

quarks and gluons in QCD. The probability of soft gluon emission is proportional to the color factor:  $C_A = 3$  for gluons and  $C_F = 4/3$  for quarks. Since  $C_A > C_F$ , gluons radiate approximately twice as many soft gluons as quarks, leading to a wider spread of energy within gluon-initiated jets. Quark jets, with less radiation, retain a more collimated structure [3, 4].

This characteristic difference in jet shapes provides a basis for distinguishing quark and gluon jets, as further explored through integrated jet shapes in the next subsection.

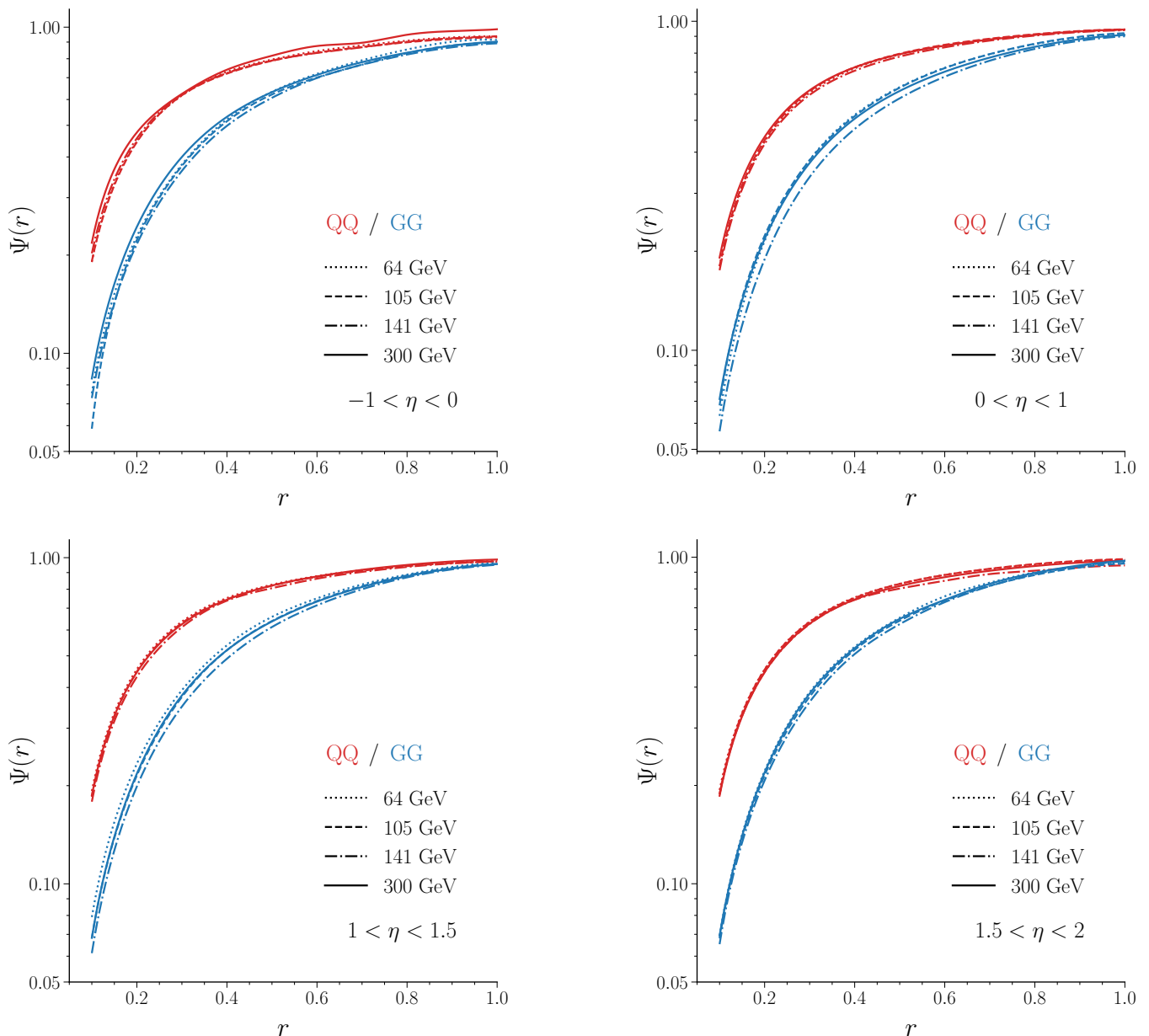


Figure 5. Integrated jet shape distribution  $\Psi(r)$  for GG (blue) and QQ (red) dijet photoproduction subsamples at different  $ep$  energies in four pseudorapidity bins:  $-1 < \eta < 0$  (top left),  $0 < \eta < 1$  (top right),  $1 < \eta < 1.5$  (bottom left), and  $1.5 < \eta < 2$  (bottom right).

## 2. Integrated Jet Shape

The integrated jet shape  $\Psi(r)$  quantifies the cumulative fraction of a jet's transverse energy contained within a cone of radius  $r$  centered on the jet axis. Unlike the differential jet shape, which measures energy in an annular ring, the integrated jet shape provides a cumulative energy profile from the jet core outward. It is defined as:

$$\Psi(r) = \frac{1}{N_{\text{jets}}} \sum_{\text{jets}} \Psi_{\text{jet}}(r) \quad (4)$$

$$\Psi_{\text{jet}}(r) = \frac{E_T(r)}{E_T(r=1)} \quad (5)$$

where  $E_T(r)$  is the transverse energy within radius  $r$  from the jet axis,  $E_T(r=1)$  is the total transverse energy within the jet cone of radius  $R=1$ , and  $N_{\text{jets}}$  is the number of jets in the sample. By definition,  $\Psi(r)$  increases monotonically from 0 at the jet axis to 1 at  $r=R$ . Figure 5 shows  $\Psi(r)$  for the GG and QQ photoproduction subsamples across four pseudorapidity intervals:  $-1 < \eta < 0$ ,  $0 < \eta < 1$ ,  $1 < \eta < 1.5$ , and  $1.5 < \eta < 2$ .

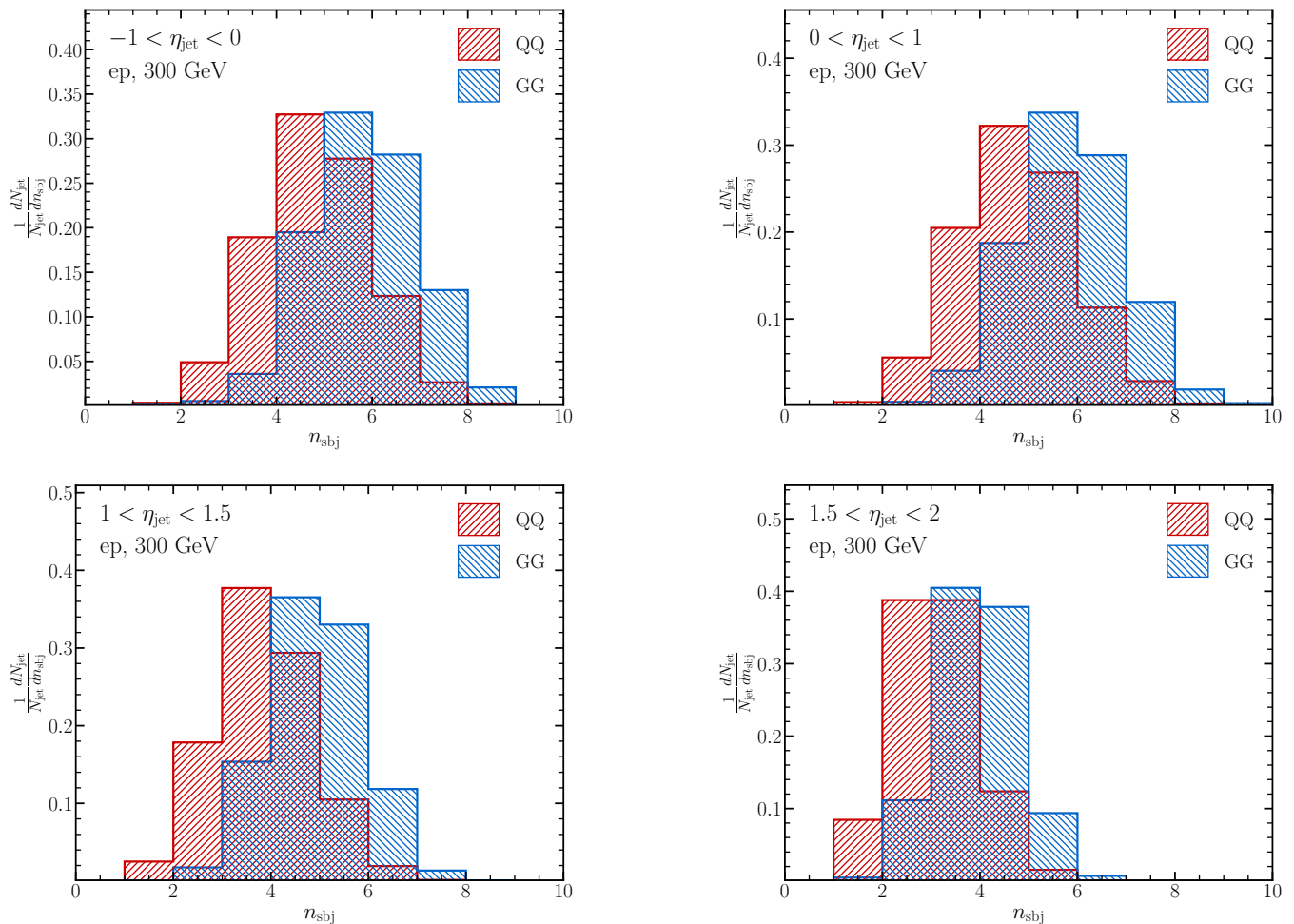


Figure 6. Subjet multiplicities for quark and gluon initiated jets for HERA ( $ep$ ,  $\sqrt{s} = 300$  GeV) in four pseudorapidity bins:  $-1 < \eta < 0$  (top left),  $0 < \eta < 1$  (top right),  $1 < \eta < 1.5$  (bottom left), and  $1.5 < \eta < 2$  (bottom right).

The distributions show the variation in transverse energy fraction radially outward from the jet axis. Quark-initiated jets exhibit a narrow energy profile, with more than 50% of the jet transverse energy concentrated within  $r = 0.3$ , as reflected by the rapidly saturating  $\Psi(r)$  curves. Gluon-initiated jets, by contrast, display a broader radial energy distribution that saturates more gradually.

This distinction is consistent across all center-of-mass energies and pseudorapidity intervals considered, indicating that the integrated jet shape profile is largely insensitive to the collision energy over the range studied. The integrated jet shape therefore serves as an effective observable for distinguishing quark- from gluon-initiated jets, as it directly probes differences in the underlying fragmentation dynamics. In the following section, we examine the subjet multiplicity, which provides complementary information on the internal structure of jets.

## B. Subjet Multiplicity

Jet substructure can be further probed by clustering the constituents within a jet into smaller subgroups called subjets. This is achieved by reapplying the longitudinally invariant  $k_T$  algorithm to the jet constituents at a finer resolution scale. Particles are successively merged until all pairwise distances satisfy the condition:

$$d_{ij} > d_{\text{cut}} = y_{\text{cut}} \cdot E_T^2 \quad (6)$$

where  $y_{\text{cut}}$  is the resolution parameter, set to  $5 \times 10^{-4}$  in this analysis. The remaining clusters at this stage are identified as subjets, and their number defines the subjet multiplicity  $n_{\text{sbj}}$  for that jet. The mean subjet multiplicity  $\langle n_{\text{sbj}} \rangle$  is then obtained by averaging over all jets in the sample. The resolution parameter  $y_{\text{cut}}$  controls the granularity at which the internal structure of a jet is probed: a smaller value resolves finer substructure, yielding a higher number of subjets, while a larger value merges nearby constituents into broader clusters. For a given  $y_{\text{cut}}$ , the subjet multiplicity is sensitive to the

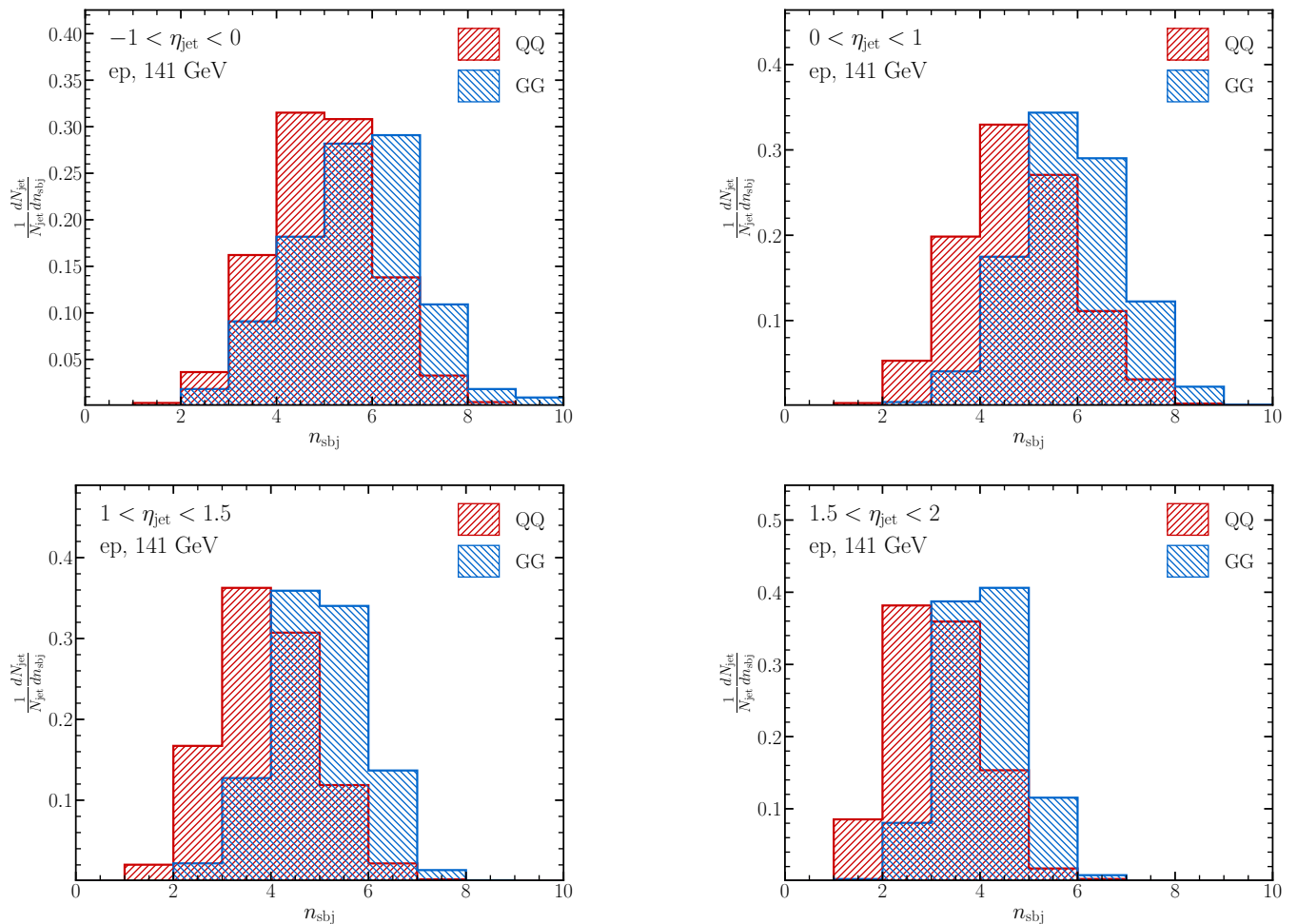


Figure 7. Subjet multiplicities for quark and gluon initiated jets for EIC ( $ep$ ,  $\sqrt{s} = 141$  GeV) in four pseudorapidity bins:  $-1 < \eta < 0$  (top left),  $0 < \eta < 1$  (top right),  $1 < \eta < 1.5$  (bottom left), and  $1.5 < \eta < 2$  (bottom right).

nature of the initiating parton. Quark-initiated jets are typically more collimated, with a narrow distribution of hadrons near the jet axis, resulting in fewer resolved subjets. Gluon-initiated jets, by contrast, exhibit a broader and more diffuse internal structure due to their higher colour charge and the correspondingly enhanced rate of soft gluon radiation.

The subjet multiplicity distributions from the GG and QQ photoproduction subsamples are shown in Figs. 6 and 7 for different pseudorapidity regions at HERA and the proposed highest EIC center-of-mass energy of 141 GeV, respectively. The mean subjet multiplicity  $\langle n_{\text{sbj}} \rangle$  for GG and QQ jets across different pseudorapidity intervals and center-of-mass energies is shown in Fig. 8.

Gluon jets consistently exhibit higher  $\langle n_{\text{sbj}} \rangle$  than quark jets, as expected from their larger color factor. To validate these simulation results, the following subsection presents a direct comparison of the integrated jet shapes with published ZEUS data [45].

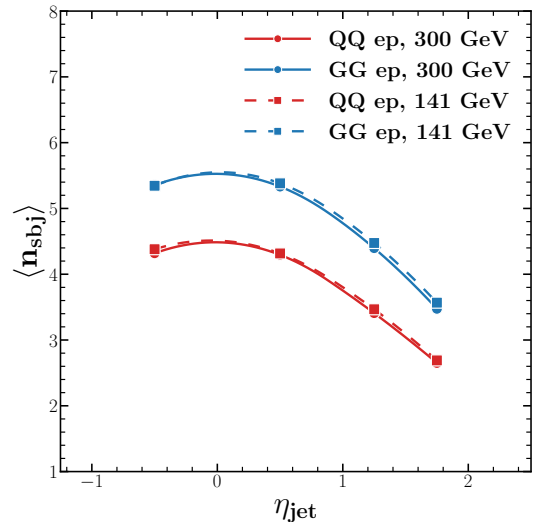


Figure 8. Mean subjet multiplicity  $\langle n_{\text{sbj}} \rangle$  as a function of jet pseudorapidity  $\eta_{\text{jet}}$  for quark (QQ) and gluon (GG) initiated dijets at  $\sqrt{s} = 141$  GeV and 300 GeV.

### C. Comparison with ZEUS data

The integrated jet shapes obtained from the simulated sample at  $\sqrt{s} = 300$  GeV are compared with the published ZEUS photoproduction data [45] in Figure 9. Since the ZEUS measurements were performed with a transverse energy threshold of  $E_T^{\text{jet}} > 17$  GeV, the same cut is applied to the simulated jets for this comparison.

In the backward pseudorapidity region ( $-1 < \eta < 0$ ), the ZEUS data points lie close to the quark jet prediction, indicating that this region is predominantly populated by quark-initiated jets. As  $\eta^{\text{jet}}$  increases, the data move progressively from the quark toward the gluon jet prediction. In the most forward interval ( $1.5 < \eta < 2.5$ ), the data fall closer to the gluon jet shape, consistent with an increasing fraction of gluon-initiated jets at higher  $\eta^{\text{jet}}$ .

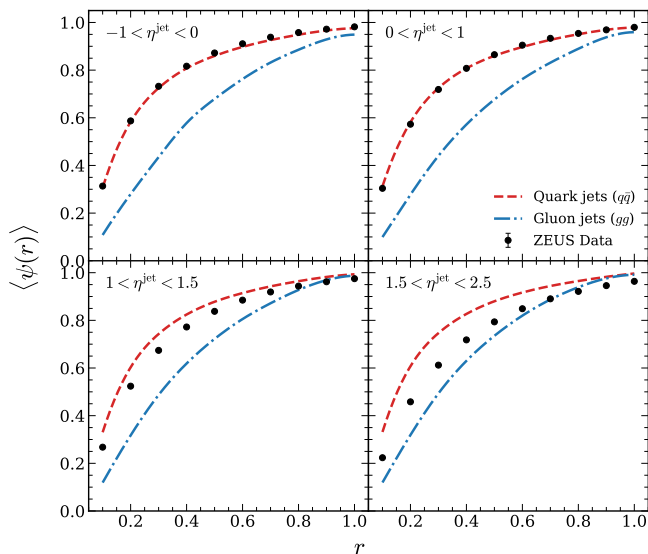


Figure 9. Integrated jet shape of quark and gluon jets with  $E_T > 17$  GeV in the simulated sample compared to published ZEUS data at  $\sqrt{s} = 300$  GeV.

This behaviour reflects the underlying parton dynamics: in the backward region, the direct process  $\gamma g \rightarrow q\bar{q}$  produces predominantly quark jets, while in the forward region, resolved processes such as  $q_\gamma g_p \rightarrow qg$  contribute an increasing proportion of gluon-initiated jets.

Figure 10 compares the integrated jet shapes at two transverse energy thresholds:  $E_T > 17$  GeV, corresponding to the ZEUS selection, and  $E_T > 10$  GeV, used in the present analysis of jet substructure at the proposed EIC energies. For both quark and gluon jets across all  $\eta^{\text{jet}}$  intervals, the integrated jet shape  $\langle \psi(r) \rangle$  reaches a higher value at small  $r$  for the higher  $E_T$  threshold and saturates closer to unity at a smaller radius. To quantify the difference, the radius at which  $\langle \psi(r) \rangle = 0.6$  is compared between the two selections. For quark jets in the backward region ( $-1 < \eta^{\text{jet}} < 0$ ), 60% of the jet transverse energy is contained within  $r \approx 0.21$  at  $E_T > 17$  GeV, compared to  $r \approx 0.28$  at  $E_T > 10$  GeV. For gluon jets

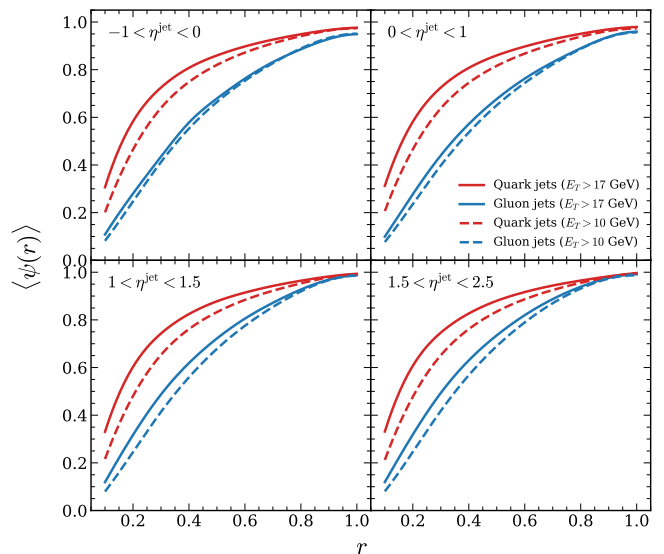


Figure 10. Integrated jet shape of the quark and gluon jets at  $E_T > 17$  GeV compared with jets at  $E_T > 10$  GeV in the simulated sample at  $\sqrt{s} = 300$  GeV.

in the same region, the corresponding radii are  $r \approx 0.42$  and  $r \approx 0.44$ , respectively. In the most forward interval ( $1.5 < \eta^{\text{jet}} < 2.5$ ), the shift is more pronounced for gluon jets, with the 60% containment radius increasing from  $r \approx 0.38$  to  $r \approx 0.43$  when the threshold is lowered. Jets selected with the higher  $E_T$  cut therefore exhibit narrower shapes, with a larger fraction of their transverse energy concentrated near the jet axis. This is consistent with the expectation from perturbative QCD that higher- $E_T$  jets are more collimated due to the reduced value of  $\alpha_s$  and the correspondingly smaller phase space for wide-angle soft gluon radiation.

These results demonstrate that jet substructure observables remain well-defined and sensitive to the quark–gluon composition even at the lower transverse energies accessible in photoproduction at the EIC, making them viable probes for further QCD studies at these facilities.

### IV. QUARK AND GLUON JET IDENTIFICATION

The differences in jet shapes and subjet multiplicities between quark and gluon jets, as presented in Section 3, suggest that these observables can be exploited for jet classification. In experimental data, however, the identity of the initiating parton is not directly accessible, and one must rely on observable jet properties to statistically distinguish quark-initiated from gluon-initiated jets. In this section, the integrated jet shape at  $r = 0.3$  is used as a simple discriminator to produce quark-enriched and gluon-enriched jet samples.

The integrated jet shape  $\Psi(r)$  at  $r = 0.3$  for the GG, QG, and QQ photoproduction subsamples at the EIC en-

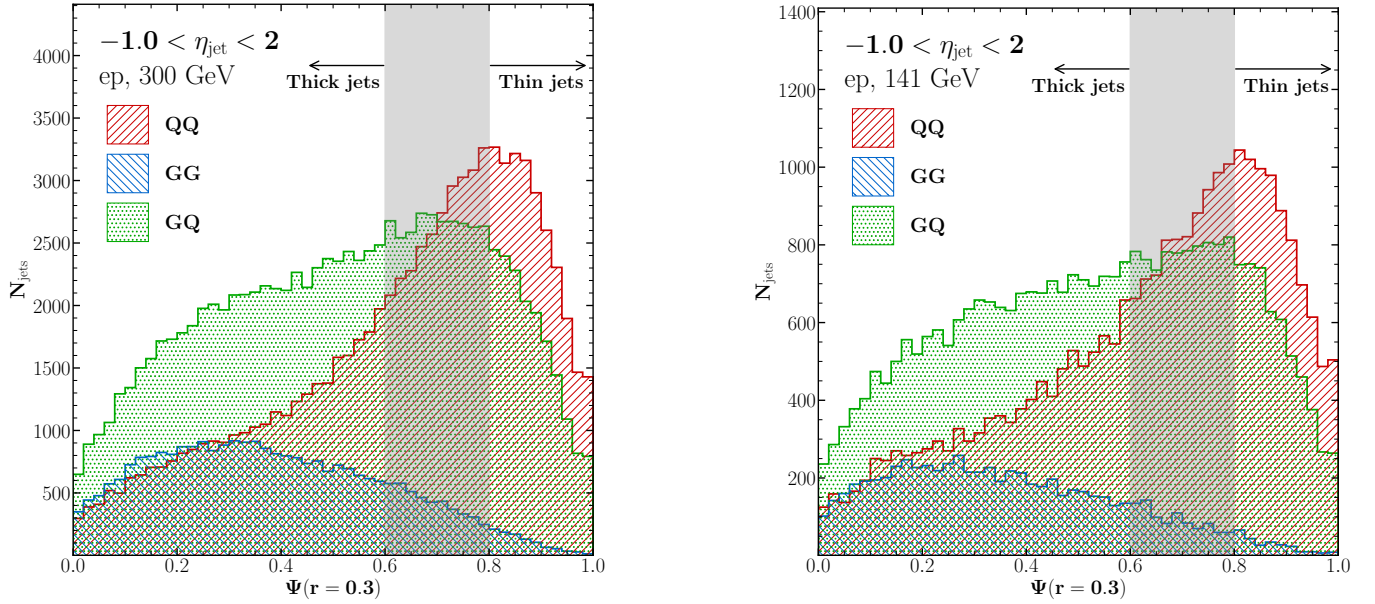


Figure 11. Integrated jet shape  $\Psi(r)$  at  $r = 0.3$  for the QQ, QG, and GG dijet photoproduction subsamples at  $\sqrt{s} = 300$  GeV (left) and  $\sqrt{s} = 141$  GeV (right).

Table IV. Percentages of thin and thick jets identified from different dijet sub-samples at EIC and HERA energies.

	EIC	EIC	EIC	HERA
$\sqrt{s}$	63.2 GeV	104.9 GeV	141 GeV	300 GeV
<b>Sample Type</b>	<b>Thin Jets (%)</b>			
QQ	64.04	62.57	61.37	53.52
GG	0.54	1.10	2.22	2.52
GQ	35.41	36.31	36.40	43.94
<b>Sample Type</b>	<b>Thick Jets (%)</b>			
QQ	39.35	34.78	26.16	26.44
GG	5.16	10.29	19.95	21.46
GQ	55.49	54.92	53.88	52.10

ergy of 141 GeV and HERA energy of 300 GeV is shown in Fig. 11. A higher value of  $\Psi(0.3)$  for the quark jet sample indicates that the transverse energy is more collimated near the jet axis. The difference in  $\Psi(0.3)$  values between the QQ and GG subsamples motivates the use of  $\Psi(0.3)$  as a jet-type discriminator. A sample enriched in quark- or gluon-initiated jets can be prepared from the generated  $ep$  photoproduction events using the following criterion.

A jet is labelled as:

- a “thin” jet, indicating a quark jet configuration, if its integrated jet shape  $\Psi(r = 0.3) > 0.8$ ;

- a “thick” jet, indicating a gluon jet configuration, if  $\Psi(r = 0.3) < 0.6$ .

These jet shape cuts are motivated by studies performed at HERA [15, 45].

Specifically, the sample with “thick” jets predominantly involves subprocesses with gluon present as the exchanged parton, such as  $gg \rightarrow gg$  and  $qg \rightarrow qg$  as shown in Table II. Conversely, the sample characterized by “thin” jets is largely dominated by subprocesses driven by quark as the exchanged parton as in the  $\gamma g \rightarrow q\bar{q}$  subprocess.

The quantitative assessment of thick and thin jet tagging in QQ, GG and QG dijet photo-production samples using the integrated jet shape is compiled in Table IV. At the lowest EIC energy of 63.2 GeV, 5.16% jets of GG sample and 55.49% of GQ sample could be labelled as the thick jets indicative of gluon partonic behaviour, whereas 39.35% of jets from QQ sample are also incorrectly labelled as thick jets. The variation in these percentages at different cm energies are shown in Table IV.

Conversely, the “thin” jets, which are linked with quark as the initiating partons in the final state, exhibit a contrasting distribution. For the lowest EIC energy of 63.2 GeV, 64.04% jets from QQ sample and 35.41% jets of GQ sample were labelled as thin jets. The incorrect identification of jets from GG sample as thin jets was found to be only 0.54%, which increases to about 2.5% at the highest EIC energy of 141 GeV.

The “thick” jets at HERA consist of 26.44% QQ, 21.46% GG, and 52.10% QG subsamples. In contrast, the “thin” jets are dominated by 53.52% QQ, 2.52% GG, and 43.94% QG subsamples. These values are comparable to the published HERA results [15], thereby validating

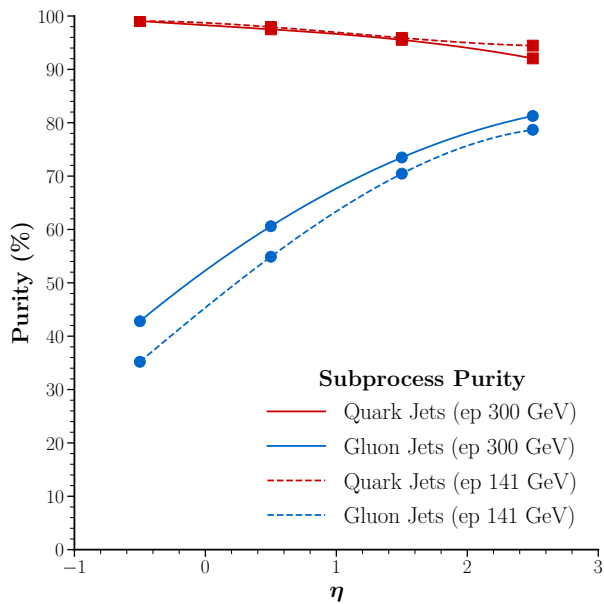


Figure 12. Purity of Quark and Gluon jets subsample selection.

ing the simulation and analysis procedures employed in this study.

### A. Purity Studies

As shown in Table IV, some false identifications occur during discrimination, and therefore the enriched samples are not 100% pure. The purity of the gluon-enriched sample, obtained by selecting thick jets with  $\Psi(0.3) < 0.6$ , is quantified as:

$$\text{Purity}_{\text{gluon}} = \frac{N_{\text{jet}}^{GG} + 0.5 \times N_{\text{jet}}^{GQ}}{N_{\text{jet}}^{GG} + N_{\text{jet}}^{QQ} + 0.5 \times N_{\text{jet}}^{GQ}} \quad (7)$$

where  $N_{\text{jet}}^{GG}$ ,  $N_{\text{jet}}^{GQ}$ , and  $N_{\text{jet}}^{QQ}$  are the number of jets from the GG, GQ, and QQ subsamples, respectively. Similarly, the purity of quark-enriched sample by selecting thin jets with  $\Psi(0.3) > 0.8$  is given by:

$$\text{Purity}_{\text{quark}} = \frac{N_{\text{jet}}^{QQ} + 0.5 \times N_{\text{jet}}^{GQ}}{N_{\text{jet}}^{GG} + N_{\text{jet}}^{QQ} + 0.5 \times N_{\text{jet}}^{GQ}} \quad (8)$$

The purity of the gluon-enriched and quark-enriched samples produced by this discriminator is shown in Fig. 12. The quark-enriched sample maintains a purity above 90% across all pseudorapidity intervals. In contrast, the gluon-enriched sample purity exhibits a strong  $\eta$  dependence, increasing from approximately 35% in the central region to about 80% in the forward pseudorapidity intervals. This trend reflects the higher gluon jet population in the forward region ( $\eta > 0$ , corresponding

to the proton beam direction), where resolved photoproduction processes dominate and gluon-initiated subprocesses such as  $qg \rightarrow qg$  are enhanced, consistent with the expected QCD dynamics in  $ep$  collisions. It should be noted that the present study is performed at the generator level; in a real detector environment with limited acceptance and finite resolution, the efficiency and purity of the selected samples would need to be re-evaluated using reconstructed data.

## V. DETECTOR OUTLOOK

The results presented above are based on generator-level simulations without detector effects. In this section, we discuss how the proposed EIC design and its detector capabilities relate to the feasibility of the jet substructure measurements presented in this work. The EIC [49] will collide electrons with protons and nuclei, providing a unique tool for studying nuclear matter and the strong interaction.

The EIC strives to attain a luminosity in the range of  $10^{33}$  to  $10^{34}$   $\text{cm}^{-2}\text{s}^{-1}$  for  $ep$  collisions and  $10^{30}$  –  $10^{32}$   $\text{cm}^{-2}\text{s}^{-1}$  for  $eA$  collisions. Within the EIC framework, electron beam energies will span from 5 to 18 GeV, while proton beam energies will range from 41 to 275 GeV, yielding center-of-mass energies from approximately 29 to 140 GeV. The accessible  $Q^2$  range in  $ep$  collisions scales with the center-of-mass energy as  $Q_{\text{max}}^2 \sim s$ . A minimum center-of-mass energy of approximately 20 GeV is required to access the perturbative regime ( $Q^2 \gtrsim 10 \text{ GeV}^2$ ) where quarks can be cleanly resolved, while center-of-mass energies of order 100 GeV are necessary to probe the high- $Q^2$  domain ( $Q^2 \gtrsim 1000 \text{ GeV}^2$ ) where electroweak effects become significant and precise determination of parton distributions at large Bjorken- $x$  is possible [49, 50].

These energy ranges will enhance sensitivity to gluon distributions, and spin-polarized beams will significantly improve our understanding of the proton's spin structure. Recent studies have demonstrated that jet substructure analysis in photoproduction events at EIC energies is viable despite typically low transverse momenta [51].

The importance of jets as probes of gluon helicity contributions to the proton spin via dijet events in DIS has been highlighted [52]. Furthermore, jet charge measurements have been proposed to classify jets by their originating partons, providing insight into nucleon flavor and spin dynamics [53, 54].

The variable center-of-mass energy, combined with the EIC's particle identification capabilities, will enable studies of hadronization processes within jets across a broad kinematic range in  $x$  and  $Q^2$ . The phase space region with pseudorapidity  $\eta > 0$  (the proton beam direction) is expected to be enriched in gluon jets, producing broader jet profiles. This forward region, accessible at the EIC, provides a promising testing ground for gluon-jet classification techniques in future data analyses.

## VI. CONCLUSION

In this study, we have investigated photoproduction processes in  $ep$  collisions at the proposed EIC energies ranging from  $\sqrt{s} = 63.2$  to 141 GeV. The analysis focuses on the substructure of jets produced through direct and resolved photoproduction processes, simulated using the PYTHIA 8 event generator. Jets are reconstructed using the longitudinally invariant  $k_T$  algorithm in FastJet 3.

In the present work, we have studied jets and their substructure in photoproduction events from electron-proton collisions across different EIC center-of-mass energies. We focused on three key observables: subjet multiplicity, differential jet shape, and integrated jet shape. This analysis allowed us to investigate the contributions of various direct and resolved photoproduction subprocesses as shown in Table II to jet formation across both EIC and HERA energies, revealing the underlying jet substructure and their energy dependencies. Dijet events were selected for a detailed comparison of jet-shapes and subjet multiplicity in the QQ and GG subsamples. The study demonstrated that gluon-initiated jets exhibit a broader, more diffused structure compared to the collimated and narrow quark-initiated jets.

The differential jet shape  $\rho(r)$  of quark jet has a larger value for small  $r$  as compared to the gluon jets, showing its transverse energy is collimated near the jet-axis and then decreases steeply. A similar observation is made by studying the integrated jet shape  $\Psi(r)$  for quark jets as compared to the gluon-initiated jets. With increasing radius, the  $\Psi(r)$  for quark jet saturates quickly, showing more than 50% energy is contained within a jet radius of 0.3. The gluon jets show a more gradual energy distribution over a larger radius. This variation can be used to identify whether the initiating parton is a gluon or a quark.

The mean subjet multiplicity of the jets in QQ and GG is studied in different pseudorapidity intervals. It is observed that the gluon jets have higher subjet multi-

plicity than the quark initiated jets in all pseudorapidity intervals at all center-of-mass energies.

We exploit the integrated jet shape variable to separate our samples into the quark and gluon jet enriched samples. The jets are labelled as thick jets if their  $\Psi(0.3)$  is less than 0.6 and as thin jets if their  $\Psi(0.3)$  is greater than 0.8, respectively. The efficiency of this variable in selecting quark jet sample is calculated and found to be more than 90%. The efficiency of this variable in producing gluon jet enriched sample is found to increase from 35% to 80% with pseudorapidity. The integrated jet shape variable  $\Psi(r)$  proves to be an effective observable to differentiate between the gluon and quark jets. The study's findings are consistent with previous observations from HERA and provide a solid foundation for future experimental investigations at the EIC.

The classification of quark and gluon jets based on their substructure is crucial for enhancing the precision of scattered parton identification. The analysis emphasizes the importance of jet substructure in probing the dynamics of parton fragmentation and hadronization processes. By leveraging the integrated and differential jet shapes, one can effectively separate quark-dominated and gluon-dominated jets, facilitating more accurate measurements and interpretations of the data.

The insights gained from this study are expected to significantly contribute to the physics program at the EIC, enabling detailed exploration of QCD phenomena and providing valuable benchmarks for tuning event generators. This, in turn, will enhance our capability to explore beyond the Standard Model physics, where new signals may be obscured by the Standard Model background. In conclusion, the detailed examination of jet substructures in photoproduction events at the EIC paves the way for more refined analyses and a deeper understanding of the strong force, parton dynamics, and the internal structure of nucleons. The aim of this paper is to highlight potentially intriguing jet-shape observables that could be utilized and further explored in detail as and when the EIC data becomes available.

- 
- [1] K. Konishi, A. Ukawa, and G. Veneziano, *Nuclear Physics B* **157**, 45 (1979).
  - [2] CMS Collaboration, A. Tumasyan, W. Adam, J. W. Andrejkovic, *et al.*, *Journal of High Energy Physics* **2022**, 188 (2022).
  - [3] R. K. Ellis, W. J. Stirling, and B. R. Webber, *QCD and collider physics*, Vol. 8 (Cambridge University Press, 2011).
  - [4] M. Tanabashi, K. Hagiwara, Hikasa, *et al.* (Particle Data Group), *Phys. Rev. D* **98**, 030001 (2018).
  - [5] OPAL collaboration, P. D. Acton, G. Alexander, J. Allison, *et al.*, *Zeitschrift für Physik C* **58**, 387 (1993).
  - [6] OPAL collaboration, R. Akers, G. Alexander, *et al.*, *Zeitschrift für Physik C* **68**, 179 (1995).
  - [7] DELPHI Collaboration, *Zeitschrift für Physik C* **70**, 179 (1996).
  - [8] ALEPH collaboration, R. Barate, *et al.*, *The European Physical Journal C* **17**, 1 (2000).
  - [9] ALEPH collaboration, D. Buskulic, *et al.*, *Physics Letters B* **384**, 353 (1996).
  - [10] ALEPH collaboration, R. Barate, B. D., *et al.*, *Physics Reports* **294**, 1 (1998).
  - [11] P. Gras, S. Höche, D. Kar, *et al.*, *Journal of High Energy Physics* **2017**, 091 (2017).
  - [12] G. Dissertori, I. G. Knowles, and M. Schmelling, *Quantum Chromodynamics: High Energy Experiments and theory* (Clarendon Press; Oxford University Press, 2009).
  - [13] A. Capella, I. M. Dremin, J. W. Gary, V. A. Nechitailo, and J. T. T. Van, *Phys. Rev. D* **61**, 074009 (2000).
  - [14] ZEUS Collaboration, S. Chekanov, M. Derrick, S. Magill, *et al.*, *The European Physical Journal C* **55**, 177 (2008).
  - [15] C. Glasman, *AIP Conference Proceedings* **571**, 203

- (2001).
- [16] J. Gallicchio and M. D. Schwartz, *Journal of High Energy Physics* **2013**, 090 (2013).
- [17] J. Gallicchio and M. D. Schwartz, *Phys. Rev. Lett.* **107**, 172001 (2011).
- [18] C. Frye *et al.*, *Physical Review D* **95**, 034001 (2017).
- [19] B. Whitmore, *Search for Beyond the Standard Model signals in a quark-gluon tagged dijet final state with the ATLAS detector*, Ph.D. thesis, Lancaster University (2019).
- [20] B. Bhattacharjee, S. Mukhopadhyay, M. Nojiri, *et al.*, *Journal of High Energy Physics* **2017**, 044 (2017).
- [21] A. Chakraborty, A. M. Iyer, and T. S. Roy, *Nucl. Phys. B.* **932**, 439 (2018).
- [22] D. Ferreira de Lima, P. Petrov, D. Soper, and M. Spannowsky, *Phys. Rev. D* **95**, 034001 (2017).
- [23] Y. Sakaki, *Phys. Rev. D* **99**, 114012 (2019).
- [24] P. T. Komiske, S. Kryhin, and J. Thaler, *Physical Review D* **106**, 014009 (2022).
- [25] P. T. Komiske, E. M. Metodiev, and J. Thaler, *Journal of High Energy Physics* **2018**, 059 (2018).
- [26] B. Bhattacharjee, S. Mukhopadhyay, M. M. Nojiri, Y. Sakaki, and B. R. Webber, *Journal of High Energy Physics* **2015**, 10.1007/jhep04(2015)131 (2015).
- [27] M. Jankowiak and A. J. Larkoski, *J. High Energy Phys.* **2011** (6).
- [28] G. Kasieczka, T. Plehn, M. Russell, and T. Schell, *J. High Energy Phys.* **2017** (5).
- [29] T. Cheng, *Comput. Softw. Big Sci.* **2**, 10.1007/s41781-018-0007-y (2018).
- [30] P. Gras, S. Höche, D. Kar, A. Larkoski, L. Lönnblad, S. Plätzer, A. Siódmok, P. Skands, G. Soyez, and J. Thaler, *J. High Energy Phys.* **2017** (7).
- [31] J. Davighi and P. Harris, *The European Physical Journal C* **78**, 334 (2018).
- [32] E. M. Metodiev and J. Thaler, *Phys. Rev. Lett.* **120**, 241602 (2018).
- [33] Z. Fodor, *Phys. Rev. D* **41**, 1726 (1990).
- [34] A. J. Larkoski, G. P. Salam, and J. Thaler, *Journal of High Energy Physics* **2013**, 108 (2013).
- [35] C. Bierlich *et al.*, *SciPost Physics Codebases* , 8 (2022).
- [36] G. P. Salam, *The European Physical Journal C* **67**, 637 (2010).
- [37] K. Rabbertz, *Jet Physics at the LHC: The Strong Force beyond the TeV Scale*, Springer Tracts in Modern Physics, Vol. 268 (Springer, Berlin, 2017).
- [38] S. Marzani, G. Soyez, and M. Spannowsky, *Lecture Notes in Physics* (2019).
- [39] J. Bonilla *et al.*, *Frontiers in Physics* **10-2022**, 10.3389/fphy.2022.897719 (2022).
- [40] S. Frixione and G. Ridolfi, *Nuclear Physics B* **507**, 315 (1997).
- [41] B. ZEUS collaboration., Chekanov, M. Derrick, *et al.*, *Physics Letters B* **649**, 12 (2007).
- [42] S. Jain, R. Aggarwal, and M. Kaur, *Phys. Rev. D* **107**, 116002 (2023).
- [43] ZEUS Collaboration, J. Breitweg, *et al.*, *The European Physical Journal C* **2**, 61 (1998).
- [44] M. Arratia, Y. Song, F. Ringer, and B. V. Jacak, *Phys. Rev. C* **101**, 065204 (2020).
- [45] B. ZEUS collaboration., Chekanov, M. Derrick, *et al.*, *Nucl. Phys. B.* **700**, 3 (2004).
- [46] S. V. Chekanov, Jet algorithms: a minireview (2002), [arXiv:hep-ph/0211298](https://arxiv.org/abs/hep-ph/0211298).
- [47] S. Catani, Y. L. Dokshitzer, M. H. Seymour, and B. R. Webber, *Nuclear Physics B* **406**, 187 (1993).
- [48] M. Cacciari, G. P. Salam, and G. Soyez, *The European Physical Journal C* **72**, 1896 (2012).
- [49] A. Accardi *et al.*, *The European Physical Journal A* **52**, 268 (2016).
- [50] R. Abdul Khalek *et al.*, *Nuclear Physics A* **1026**, 122447 (2022).
- [51] M. Klasen and K. Kovařík, *Phys. Rev. D* **97**, 114013 (2018).
- [52] B. S. Page, X. Chu, and E. C. Aschenauer, *Phys. Rev. D* **101**, 072003 (2020).
- [53] Z.-B. Kang, A. J. Larkoski, and J. Yang, *Phys. Rev. Lett.* **130**, 151901 (2023).
- [54] Z.-B. Kang, X. Liu, S. Mantry, and D. Y. Shao, *Phys. Rev. Lett.* **125**, 242003 (2020).